

# Photochemical silver nanoparticles deposition on sol–gel TiO<sub>2</sub> for plasmonic properties utilization

Z. Starowicz · M. Lipiński · R. P. Socha ·  
K. Berent · G. Kulesza · P. Ozga

Received: 13 June 2014 / Accepted: 21 September 2014 / Published online: 9 October 2014  
© The Author(s) 2014. This article is published with open access at Springerlink.com

**Abstract** This paper shows investigations on silver nanoparticles deposition using simple photochemical method on sol–gel coated titania. The influence of titania substrate, silver precursor concentration, light intensity and irradiation time are considered as a factors determining the microstructure. The average diameter of the particles and surface coverage are calculated from SEM microstructure investigations and confirmed by AFM imaging. The crystalline phase in titania layers were determined by TEM and Raman spectroscopy. The optical measurements of absorbance and absorption were shown indicating that there was no absorption of the light used in experiment even though deposition of nano silver was confirmed. Finally, the plasmonic properties were simulated for the model particles by finite difference time domain method. Possible application of obtained structure was proposed.

**Keywords** Silver nanoparticles · Plasmonics · Photochemical deposition · Titanium dioxide

## 1 Introduction

Silver nanoparticles have found an application in several fields of science and technology like nanobiology, nanochemistry and materials science. The photochemical deposition is one of the methods where silver nanoparticles can be successfully formed and deposited on different surfaces [1–3]. This method was successfully used to obtain Surface Enhanced Raman Spectroscopy (SERS) effect on active nanoparticles [4], antibacterial coatings [5] and enhanced water purification [6]. Recent years have shown particular interest in utilization of silver nanoparticles and their plasmonic properties. The surface plasmons are collective oscillations of free electrons in metals. In case of nanoobjects those collective oscillations can be excited by electromagnetic radiation and for certain frequency they can show a resonance character, so called Localized Surface Plasmon Resonance (LSPR), which is the source of new optical phenomena. Silver is a metal of strong surface plasmon resonance, which, in case of the silver nanoparticles, occurs in the visible part of electromagnetic spectrum. Since the plasmonic properties of particle depend on kind of metal, its size, shape and dielectric environment, the position and character of plasmon peak can be tuned in the wide range of spectrum. The area on which particle interact with light can be assessed by extinction cross section according to for example Mie theory or Quasistatic approximation. Special feature of LSPR is that the extinction cross section several times exceeds the geometrical cross section of the particles. Extinction cross section is the sum of scattering and absorption cross sections. Depending on size one of two components dominates. Generally, the silver particles with size lower than 70 nm strongly absorb the light, while for particles larger than 70 nm, the scattering predominates [7]. Another phenomenon accompanying the LSPR is near

---

Z. Starowicz (✉) · M. Lipiński · G. Kulesza · P. Ozga  
Institute of Metallurgy and Materials Science, Polish Academy  
of Sciences, Reymonta 25, 30-059 Cracow, Poland  
e-mail: zbigniew.starowicz@gmail.com

R. P. Socha  
Jerzy Haber Institute of Catalysis and Surface Chemistry, Polish  
Academy of Sciences, Niezapominajek 8, 30-239 Cracow,  
Poland

K. Berent  
Academic Centre for Materials and Nanotechnology, AGH  
University of Science and Technology, Mickiewicza 30,  
30-059 Cracow, Poland

electric field enhancement at the close vicinity of particle surface. In recent years there has been particular interest in application of plasmonic structures in photovoltaic devices. Atwater et al. [8] proposed different possibility of plasmonic particles applied in the solar cells. Larger nanoparticles could be placed either on front or back side of the cell providing angular light scattering and hence light trapping for optical losses reduction. In the second approach, the nanoparticles are placed inside the active layer where enhanced near electric field results in increase of the electron–hole pair generation. For those purposes a high density of particles at the surface is necessary. The aim of this work was investigation of silver particle arrays deposition by photochemical method. It is a simple and cheap method with high potential of industrial application. In our approach, TiO<sub>2</sub> was used as a substrate. The titanium dioxide, widely used in solar cells in different configurations like layered structures or the powder ones. In organic or polymer solar cells, TiO<sub>2</sub> is an electron transporting layer whereas in silicon devices its antireflection properties are utilized.

Beck et al. [9] has shown that TiO<sub>2</sub> would be applicable as an under layer in plasmonic back reflector concept. Therefore, we planned to deposit either small and large particles to enable both strong near field enhancement and the scattering behaviour, respectively. For that purpose, the properties of titanium dioxide substrate were also investigated.

## 2 Experimental

The titanium oxide layer, as a substrate for silver nanoparticle deposition, was prepared by sol–gel method. The sol was a mixture of 50 ml of ethanol, 1 ml of 40 % hydrochloric acid and 5 ml of titanium (IV) ethoxide (C<sub>8</sub>H<sub>24</sub>O<sub>4</sub>Ti) precursor (Merck). The sol was conditioned for 15 min after mixing of the compounds. The monocrystalline silicon wafers and microscopic glass slides were used as the substrates. Standard cleaning procedure (sonification in acetone bath, ethanol and deionized water for 5 min) was applied. Then the sol was deposited on silicon wafers by spin-coating for 15 s with 4,000 rpm. Subsequently, the thermal treatment was applied. The samples were dried for 2 h at 100 °C in ambient atmosphere followed by calcination in flowing oxygen at 500 °C for 1 and 2 h [10]. Additionally, one other sample was annealed at 200 °C for 15 min. The TiO<sub>2</sub> spin-coated layer calcined at 500 °C for 2 h was chosen for silver deposition. On the basis of Paunovic et al. [11], which wrote that light with wavelength shorter than ~410 nm can be successfully used for photochemical silver deposition on titanium dioxide, the 405 nm point diode laser with 50 mW nominal power was

chosen. The silver precursor was silver nitrate solution of 5 different concentrations: 10, 5, 2, 1 and 0.5 mM. The temperature of silver nitrate solution was stabilized at 25 °C. During the experiments, the samples were immersed into the silver salt solution and irradiated with three levels of intensity (low, medium, high) in the dark room. The 3.2 Carl Zeiss objective lens was placed 20 cm above the sample level to provide laser beam broadening. The illuminated area of about 0.25 cm<sup>2</sup> was a oval shaped. The samples were placed inside the illuminated area to obtain uniform light intensity. The same beaker and solution volume was used in every experiment to ensure the same optical path of the beam through solution (about 1 cm). To investigate the initial stage of Ag particles formation, the irradiation time was fixed at 5 min and for larger nanoparticles deposition, the time was prolonged. The deposition was performed on substrates after different heat treatment described above.

The microstructure investigation was performed by scanning electron microscope (SEM, Versa 3D FEG) operating at an acceleration voltage of 5 kV. The statistical information was calculated by Loco's Shire software [12] from images (BSE). In order to avoid accidental and false particles selection the threshold of nanoparticle diameter was selected at 10 nm. The images before the particles analysis were subjected to the series of advanced decomposition procedures, which enable to distinguish particle contrast. The TiO<sub>2</sub> layers after different heat treatment were optically characterized in reflection, transmission and absorbance mode using Perkin Elmer Lambda 950S spectrophotometer equipped with integrating sphere. Absorbance of silver salt solution was measured as well. The refractive index and layer thickness of the investigated samples was determined using Spectroscopic Ellipsometer SE 800 PV (SENTECH) by at incidence angle of 70°. The Micro-Raman spectra were acquired using a Renishaw inVia Raman microscope (50× objective) with 633 nm HeNe excitation laser, 1 s exposure time, 50 accumulations (2,000 for detailed analysis), with 50 % laser power (21 mW output power) and with spatial resolution <1 μm. The structure and morphology of the layers was characterized by transmission electron microscopy (TEM) Tecnai G2 F20 at 200 kV. The surface composition and electronic states of elements were determined by X-ray Photoelectron Spectroscopy (XPS) with R4000 GammaData Scienta analyser and Al Kα (1,486.7 eV, 13 kV, 14 mA) X-ray source. An analysis of the nanoparticle shape and size was performed in tapping mode by Atomic Force Microscopy (AFM) (Bruker Innova). The step size was adjusted to match the image resolution and tip radius. Resulting data were used for plasmonic properties simulations, performed in Lumerical's FDTD Solution 8,0 software, which allowed calculation of the electromagnetic field evolution in time.

**Fig. 1** SEM images of microstructure of samples prepared at different light intensity and concentration of silver solution C: **a** low intensity, C = 0.5 mM, **b** high intensity, C = 0.5 mM, **c** medium intensity, C = 5 mM, **d** low intensity, C = 10 mM, **e** high intensity, C = 10 mM

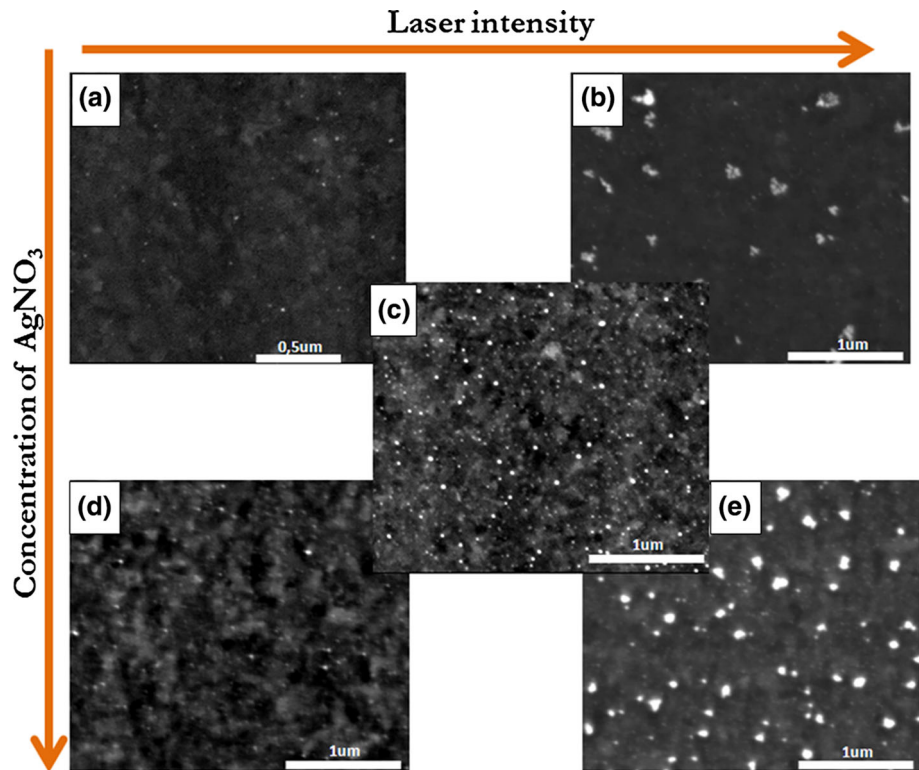


**Table 1** Average particle diameter according to different preparation condition, ± standard deviation

| Concentration [mM] | Diameter of silver particle [nm] |                  |                |
|--------------------|----------------------------------|------------------|----------------|
|                    | Low intensity                    | Medium intensity | High intensity |
| 0.5                | 17.1 ± 6.2                       | 23.1 ± 10.9      | 32.9 ± 30.3    |
| 1                  | 18.9 ± 7                         | 19.3 ± 7.7       | 27.7 ± 21.5    |
| 2                  | 17.4 ± 7.6                       | 19.0 ± 8         | 39.8 ± 29      |
| 5                  | 20.9 ± 16.5                      | 25.7 ± 8.7       | 39.1 ± 26.7    |
| 10                 | 19.7 ± 8                         | 29.4 ± 12.5      | 32.1 ± 22.2    |

**Table 2** Average particles surface coverage according to different preparation condition, ± standard deviation

| Concentration [mM] | Surface coverage [%] |                  |                |
|--------------------|----------------------|------------------|----------------|
|                    | Low intensity        | Medium intensity | High intensity |
| 0.5                | 0.30 ± 0.12          | 0.31 ± 0.1       | 2.20 ± 0.5     |
| 1                  | 1.4 ± 0.31           | 0.92 ± 0.28      | 3.02 ± 1.71    |
| 2                  | 1.34 ± 0.77          | 1.54 ± 0.44      | 1.77 ± 0.28    |
| 5                  | 1.21 ± 0.67          | 1.27 ± 0.6       | 2.48 ± 0.76    |
| 10                 | 1.15 ± 0.49          | 2.01 ± 0.38      | 4.14 ± 0.82    |

### 3 Results and discussion

#### 3.1 Particles analysis

The silver particles were deposited on TiO<sub>2</sub> surface. Then the morphology and particle size were analysed by SEM. The SEM images shown in Fig. 1 were subjected to computer analysis using Loco’s Shire graphical software. Some of the particles were hardly visible on the images due to the background contrast, which is ascribed to different crystallographic orientation of substrate grains. In order to perform statistical analysis, every image was deconvoluted using, so called, wavelet decomposition and colour normalisation. On that basis, the average diameter of the particles and average surface coverage was determined for

all silver precursor concentrations and light intensities (Tables 1, 2). The real area of the particles was converted to diameter of equivalent sphere.

The analysis of SEM images showed that diameter of silver particles obtained after 5 min of irradiation was in most cases smaller than 30 nm. Increase of silver nitrate concentration led to higher number of particles per unit area. Additionally, an increase of light intensity resulted in higher particle density as well as formation of larger particles. There are also derogations from the foregoing statements, which can be caused by inhomogeneity of the light intensity. Namely, when the high laser light intensity was used, the nanoparticles displayed irregular shapes and larger size distribution, which was emphasized at lower salt concentration. The latter result disqualified the highest

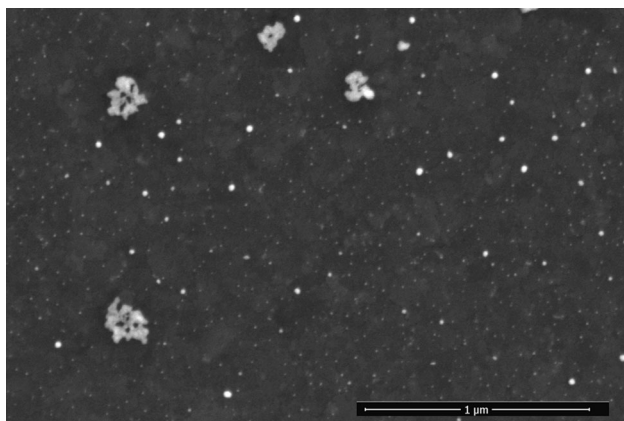
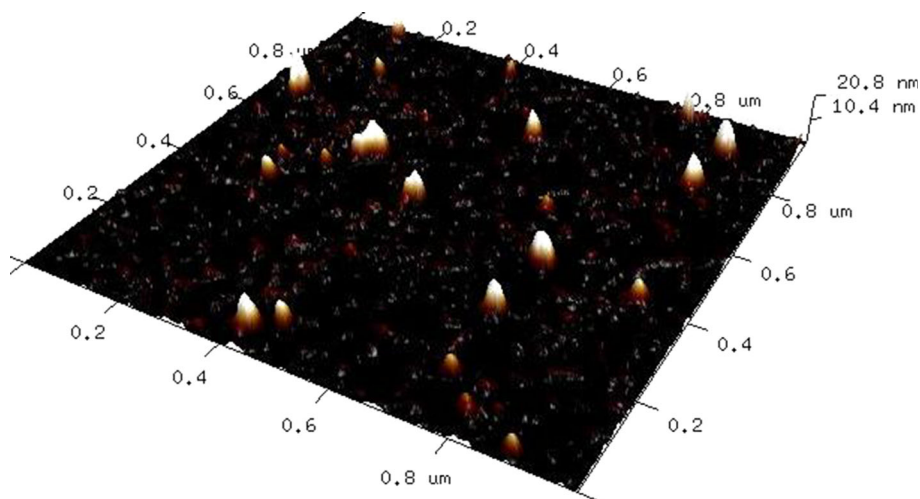


**Fig. 2** SEM image of sample irradiated for 20 min

level of light intensity for any further use. According to the mentioned plasmonic properties such small nanoparticles obtained after 5 min of irradiation should display absorbing behaviour predominantly. In order to approach the regime where the light scattering dominates, the particles must be larger. For that matter sample was placed in 5 mM of  $\text{AgNO}_3$  solution and irradiated with medium intensity for 20 min.

As can be seen from Fig. 2, the prolongation of exposure time resulted in inhomogeneous growth of some particles of irregular shape when most of the particles remained small. The bimodal particle size distribution was also observed. That indicated that it was not possible to obtain larger particles by a simple time extension. The silver deposition tests on  $\text{TiO}_2$  surfaces subjected to different heat treatment revealed that nanoparticles deposited only on substrates calcined at  $500^\circ\text{C}$ , independently of the annealing time. For further investigations, two samples were prepared in 5 and 10 mM of  $\text{AgNO}_3$  and irradiated for 5 min with medium light intensity. The AFM imaging of  $\text{Ag}/\text{TiO}_2$  system obtained at lower salt concentration was

**Fig. 3** AFM 3D topography map of sample at medium intensity,  $C = 5$  mM



performed. The surface of system obtained at higher silver slat concentration was analysed by XPS.

AFM imaging showed that the average diameter of the particles, calculated using Loco's Shire software, was 31 nm and the average particle's height ( $h$ ) was about 12 nm (Fig. 3).

This diameter was larger than the value obtained from SEM image analysis (25.7 nm). It is well known [12] that AFM gives excellent resolution in  $z$  axis but suffers from lower resolution in  $x$  and  $y$  axis. For higher resolution imaging, a special type of super sharp tips was employed. The tip was TESP SS type from Bruker, which has a radius of about 2 nm. After introduction correction of measured diameter ( $D$ ), the height ( $h$ ) of the measured object and the tip radius ( $R$ ) [13] according to Eq. (1), the average diameter ( $d$ ) was accepted as 28 nm. This resulted in the average height to radius ratio ( $h:d/2$ ) of about 0.86.

$$d = (D^2 - 8Rh)^{0.5} \quad (1)$$

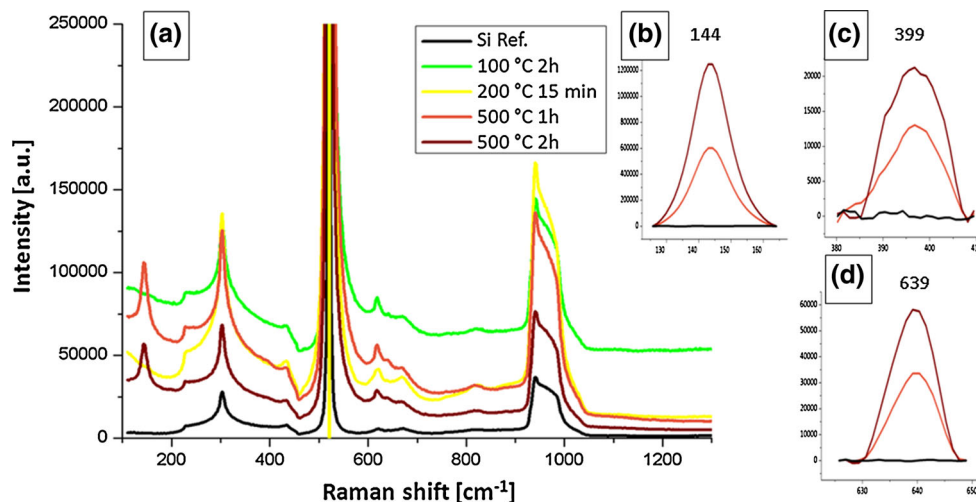
On that basis, the AFM measurements can be considered as a validated thus the values obtained from SEM should be scaled by the factor of 1.1. Some advantage of SEM using was possibility to obtain statistical information from any location in relatively short time.

### 3.2 $\text{TiO}_2$ layers investigations

Raman spectroscopy was used for phase identification in  $\text{TiO}_2$  layers prepared by sol-gel method. Analyzing the Raman spectra of titanium oxide on Si after different heat treatment (Fig. 4a) one can observe a peak at  $144\text{ cm}^{-1}$  only for the samples annealed at  $500^\circ\text{C}$ . This peak, which was not observed for the samples annealed at lower temperatures, indicated appearance of some crystalline phase. Among 6 characteristic peaks for anatase phase, which could be found at 144, 197, 399, 515, 519,  $639\text{ cm}^{-1}$  [14],



**Fig. 4** **a** Raman spectra of titania layers calcined at different temperatures, detailed analysis anatase characteristic peaks at **b–d**



the peak at  $144\text{ cm}^{-1}$  has the highest intensity (Fig. 4b). Detailed analysis with increased number of accumulations revealed also presence of the peaks at  $399$  (Fig. 4c) and  $639\text{ cm}^{-1}$  (Fig. 4d). The peaks  $515$  and  $519$  could not be distinguished from the silicon substrate peak, while the peak at  $197$  wasn't evident from the background. Beside the peak at  $144\text{ cm}^{-1}$ , which could be ascribed to both rutile and anatase, no peaks at  $447$ ,  $612$ ,  $826$  [15] that could indicate a rutile phase, were found.

The TEM analysis was employed search for a phase composition of the titania coating as well. The focused ion beam was used for preparation of thin foil specimen from the sample annealed at  $500\text{ °C}$  for  $2\text{ h}$  that already showed a presence of crystalline titania phase. Thin specimen was then analyzed by transmission electron microscopy for the phase identification (Fig. 5). On the basis of electron diffraction pattern a phase analysis was performed. This confirmed that the observed phase is anatase. From the electron diffraction pattern additional information was obtained. Thereafter an individual diffraction rings blur and slight broadening was noticed. Thus one could deduce that the studied layer is only partially (without quantitative analysis) crystallized. In the diffraction image, some spots were found on the diffraction rings. This was a result of diffraction on silicon monocrystalline substrate, due to the used aperture which disabled diffraction only from the thin titania layer. Approximation of the layer thickness was carried out by the chemical composition analysis since bright field images didn't show it exactly. Thickness of the layer was about  $50\text{ nm}$ . The phase analysis was in agreements with literature announcement of nanopowders obtained by sol–gel method that amorphous in phase but with increasing the temperature up to  $350\text{ °C}$  or higher the transition from amorphous to anatase phase happens. However, calcination temperature must be kept lower than  $600\text{ °C}$ , because of the phase transition from anatase to

rutile phase [16]. The phase identification was important since it determined the optical properties.

Rutile has a band gap  $E_g$  of  $3.0\text{ eV}$ , which corresponds with  $413\text{ nm}$ , while anatase band gap is  $3.2\text{ eV}$ , which corresponds to  $387\text{ nm}$ . The value given in [11] was probably chosen for rutile but in our samples, anatase was the occurring phase, therefore the light wavelength of  $405\text{ nm}$  used in the experiment should not be absorbed. Thus the classical photochemical mechanism of silver reduction did not occur in this case but the silver nanoparticles deposition was observed.

The XPS technique allowed determining the electronic states of Ag and Ti at the studied surface. The Ag/Ti atomic ratio was  $0.13$  ( $0.5\text{ at.}\%$  at the surface), confirming that only part of the  $\text{TiO}_2$  surface was covered by silver. The Ti  $2p$  core excitation (Fig. 6a) was deconvoluted into two components at electron binding energies (BE) of  $457.1$  and  $458.6\text{ eV}$ , respectively. The main component of  $93.6\%$  intensity was assigned to  $\text{Ti}^{4+}$  in  $\text{TiO}_2$  lattice and the lower one ( $6.4\%$ ) to  $\text{Ti}^{4+}\text{-O-C}$  of unhydrolyzed titanium (IV) precursor [17, 18]. The Ag  $3d$  spectrum was deconvoluted into three doublets where the main Ag  $3d_{5/2}$  peak ( $80.7\%$  of the intensity) at BE of  $367.7\text{ eV}$  was ascribed to metallic silver. The component at BE of  $366.9\text{ eV}$  ( $11.8\%$ ) was assigned to  $\text{Ag}^+\text{-O}$  bonding in silver oxide and the one at  $369.1\text{ eV}$  ( $7.5\%$ ) to  $\text{Ag}^+$  in salts or organic compounds [17, 18]. The XPS analysis showed that dispersed silver particles are metallic in bulk and covered by thin oxide layer at the interface.

Absorbance and absorption of the  $\text{TiO}_2$  layers after annealing on glass substrate was measured for  $300\text{--}1,100\text{ nm}$  of light wavelength (Fig. 7).

The measurements showed absorption in shortest wavelength range, which approximately ends up with high slope around  $350\text{--}360\text{ nm}$ . Then for longer wavelengths, a very broad and low intensity absorbance peak appeared.

**Fig. 5** TEM images of TiO<sub>2</sub> layer annealed at 500 °C for 2 h: up—bright field and electron diffraction, down—STEM image and composition line scan

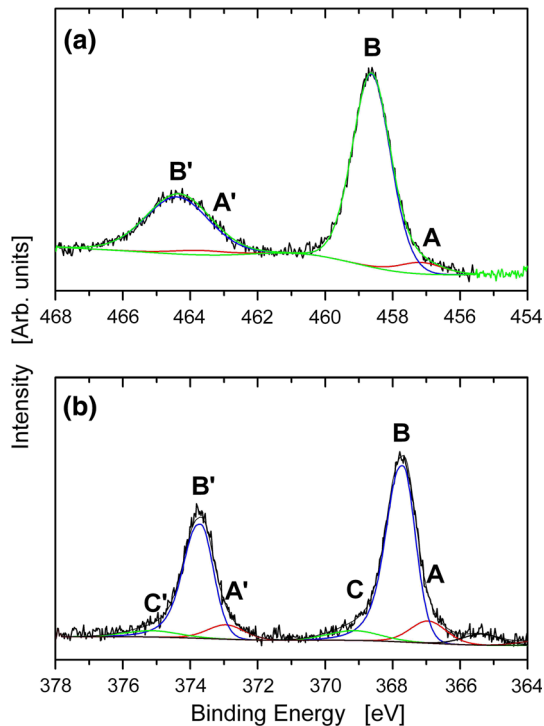
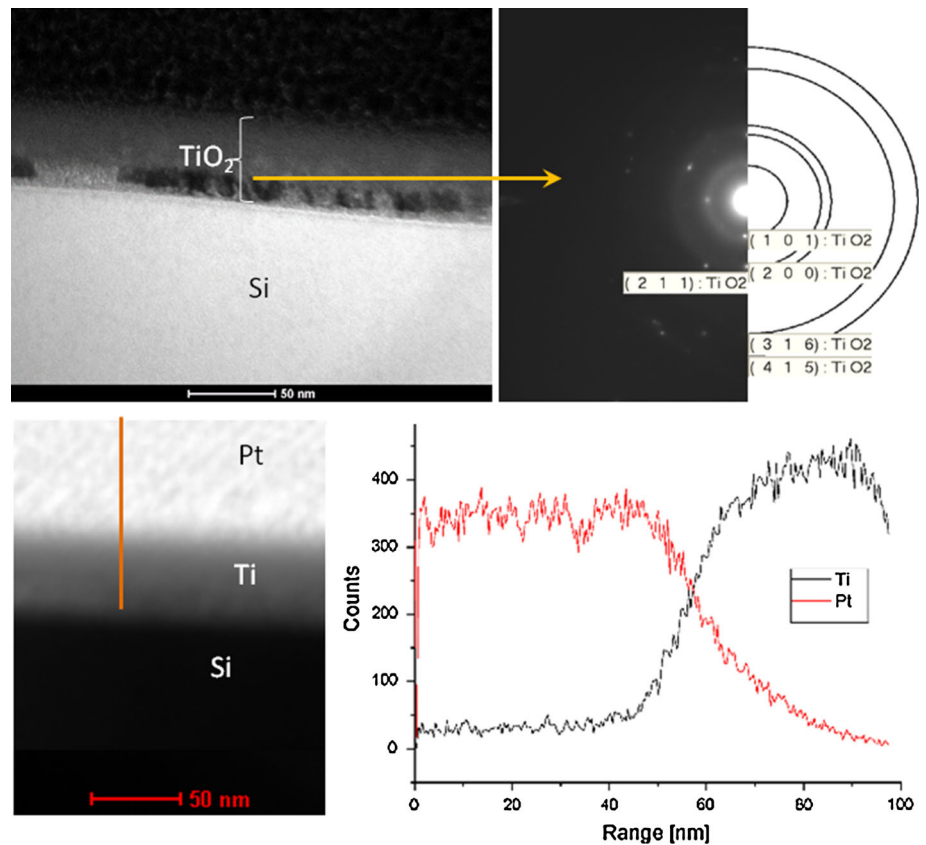


**Fig. 6** The deconvoluted Ti 2p **a** and Ag 3d **b** core excitations for Ag/TiO<sub>2</sub> sample

When the curves for differently annealed samples were compared, there was no difference between those calcined at 100 and 200 °C, which differed significantly from those annealed at 500 °C. The comparison of results for the samples calcined at 500 °C for 1 and 2 h revealed that the calcination time did not influence the optical properties and can be shortened. On the basis of the absorbance measurements one can observe that absorption occurs at 405 nm. Absorbance was calculated from Eq. (2), where  $I$  is the intensity of the measuring beam and  $I_0$  is the reference beam intensity.

$$Abs = -\log\left(\frac{I}{I_0}\right) \quad (2)$$

It relayed on only simple intensity decrease but without distinguishing the source of this decrease. It can be absorption, but in layers measurements also reflection causes decrease of the measuring beam intensity. Since titania layer certainly reflects more light than pure glass due to the higher refractive index and it can be source of second broad absorbance peak. Calculation of absorption A from Eq. (3) using the transmission T and reflection R measurements confirmed that there is no absorption of light of 405 nm in the titania layer.

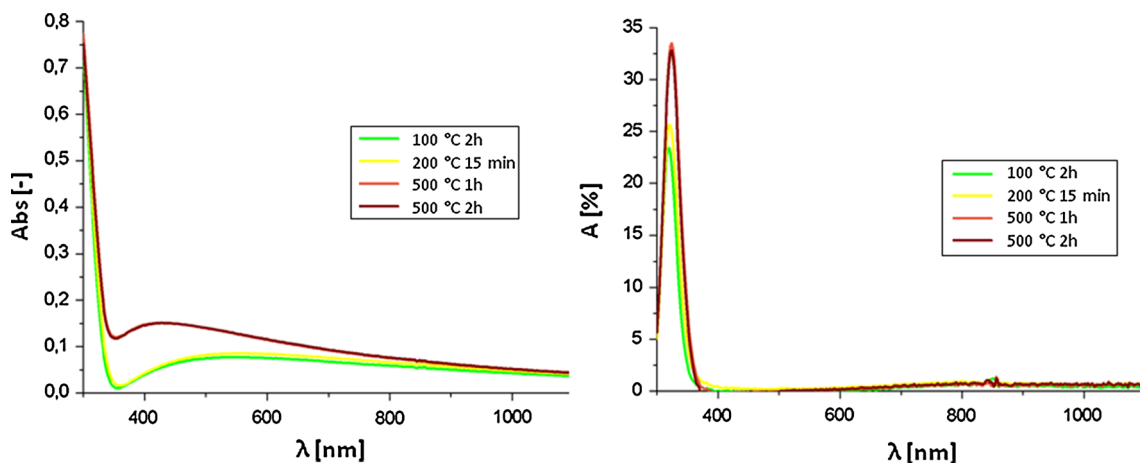


Fig. 7 Optical parameters of titania layers: Absorbance (left), Absorption (right)

Table 3 The thickness and optical parameters obtained by ellipsometry for all samples

|                           | 100 °C<br>2 h | 200 °C<br>15 min | 500 °C<br>1 h | 500 °C<br>2 h |
|---------------------------|---------------|------------------|---------------|---------------|
| Thickness (nm)            | 73            | 67               | 53            | 53            |
| n (580 nm)                | 2.02          | 2.06             | 2.25          | 2.26          |
| k < 10 <sup>-4</sup> (nm) | 346           | 351              | 361           | 361           |

$$A = 100 - R - T [\%] \tag{3}$$

Absorbance of silver nitrate solution did not confirm absorption of 405 nm light in the solution.

The ellipsometry was then used for optical dispersion characterization. For modelling of the ellipsometry results, a model consisting of silicon (100) substrate, native silicon dioxide of fixed thickness of 2 nm, titanium oxide approximated by Tauc-Lorentz model, roughness and air was applied. The best fits were obtained with mean square error below 1. The thickness of the titanium oxide layer after calcined at 500 °C for 2 h was 53 nm, which was in good agreement with thickness obtained from TEM investigations. For the samples annealed at lower temperatures, the thickness was larger. The obtained thicknesses and other optical parameters determined from ellipsometric measurements were collected in Table 3.

An analysis of the obtained extinction coefficient *k* functions allowed determination of the optical absorption edge at the wavelength, at which its value was below 10<sup>-4</sup>. And again those values were found below 405 nm, which was used in silver deposition experiments. Surprisingly, the slope end of titania absorbance curve and extinction coefficient that determined absorption edges were below the values expected for anatase phase. This feature could be related to the fact that layer in not perfectly crystallized.

The above presented results suggested that classical photochemical mechanism of silver deposition cannot be applied here in a simple way. Therefore, three possible effects could be taken into account to explain silver deposition: (1) direct transfer of the excited electron from titanium oxide valance band to adsorbed on the surface silver cation due to the redox potentials difference, which enabled transmission of lower energy than the E<sub>g</sub>, (2) transfer of electrons through the defects levels, (3) surface effects related to band bending. An explanation of these effects and their importance requires further analysis and is beyond the scope of this paper.

### 3.3 Plasmonic properties estimation

The FDTD Solution simulation software was used for estimation of the plasmonic properties of the silver nanoparticles. In the modelling, the particle (r = 14 nm, h = 12 nm) was placed on TiO<sub>2</sub> substrate within the measuring mesh of a step 0.5 nm. The optical data for silver was taken from Palik [19] references and for TiO<sub>2</sub>, from ellipsometric measurements. The scattering and absorption cross section were normalized by geometrical cross section (Fig. 8).

The simulations for silver particle showed that the LSPR position is strongly red shifted to ~612 nm when compared to spherical particle in air (LSPR around 350 nm). This shift resulted from the hemispherical shaped particle and contact with high refractive index substrate. An analysis of the near field intensity (calculated as |E<sup>2</sup>) for resonance wavelength (Fig. 8b) in polarisation plane shown that electric field can be enhanced more than 1,000 times at specific places. In case the light propagation was along horizontal direction and oscillation of the electric field in vertical directions. The colour scale was adjusted from the minimal and maximal values of electric field intensity

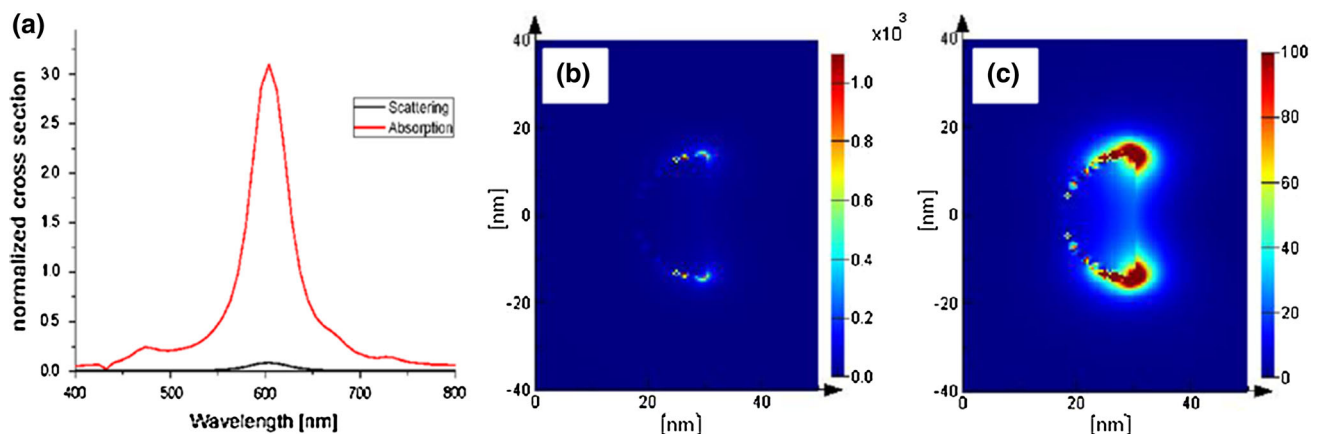


**Fig. 8** The results of plasmonic properties simulation: **a** normalized absorption and scattering cross section for particle diameter of  $r = 14$  nm and  $h = 12$  nm particles, **b** near field enhancement at  $\lambda = 612$  nm, **c** range of 100 times field enhancement at  $\lambda = 612$  nm

enhancement. In the Fig. 8c, the field enhancement was fixed on 100 times and it was shown that the electric field is enhanced only a distance of few nm from the particle surface. Above information are quite optimistic and shows the possibility of using those nanoparticles in so called inverted organic solar cells with  $\text{TiO}_x$  layer [20], where the particles could interact with light, which is weakly absorbed in the active layer. Small height of the particles is also an advantage since the active layer penetration is important parameter as shown by Chen et al. [21].

#### 4 Summary

Photochemical deposition of silver nanoparticles can be convenient method to utilize their plasmonic properties. Deposition parameters strongly influence the microstructure and particles morphology. So far this method enables the formation of the small nanoparticles (<50 nm). On the basis of computer simulation, redshift of LSPR position and strong near field enhancement at the particles surface is expected. To take full advantage of particles properties deposition parameters should be still carefully studied and optimised. Considering the optical measurements results it was shown that particles are deposited even when there is no absorption of 405 nm radiation. It raises the question about the mechanism of photochemical deposition that needs further studies.

**Acknowledgments** This research was support by European Union within European Social Fund realization under the project No. POKL.04.01.01-00-004/10 ‘Interdisciplinary PhD Studies in Materials Engineering with English as the language of instruction’. The SEM examination was performed in the Accredited Testing Laboratory of the Institute of Metallurgy and Materials Science of the Polish Academy of Sciences in Cracow. The computer simulation and simulation software was funded by the Polish National Science Centre on the basis of the decisions number DEC-2012/05/B/ST8/00087.

**Open Access** This article is distributed under the terms of the Creative Commons Attribution License which permits any use, distribution, and reproduction in any medium, provided the original author(s) and the source are credited.

#### References

- Zolfaghari Borra M, Kayra Güllü S, Es F, Demircioğlu O, Günöven M, Turan R, Bek A (2014) *Appl Surf Sci*. doi:10.1016/j.apsusc.2013.12.088
- Oćwieja M, Adamczyk Z (2013) *Langmuir* 29:3546–3555
- Nychyporuk T, Zhou Z, Lemiti M, Bastide S (2010) *Sol Energy Mater Soc Cells* 94:2314–2317
- Kudu S, Mandal M, Kumar Ghosh S, Pal T (2004) *J Colloid Interface Sci* 272:134–144
- Pollini A, Paladini F, Catalano M, Taurino A, Licciulli A, Maffezzoli A, Sannino A (2011) *J Mater Sci Mater Med* 22:2005–2012
- Wodka D, Bielańska E, Socha R, Elźbieciak-Wodka M, Gurgul J, Nowak P, Warszyński P, Kumakiri I (2010) *ACS Appl Mater Interfaces* 2(7):1945–1953
- Temple TL, Mahanama GDK, Reehal HS, Bagnall DM (2009) *Sol Energy Mater Sol Cells* 93:1978–1985
- Atwater H, Polman A (2010) *Nat Mater* 9:205–212
- Beck FJ, Polman A, Catchpole K (2009) *J Appl Phys* 105:114310
- Piwoński I, Kądzioła K, Kisielewska A, Soliwoda K, Wolszczak M, Lisowska K, Wrońska N, Felczak A (2011) *Appl Surf Sci* 257:7076–7082
- Paunovic M, Schlesinger M (2006) *Fundamentals of electrochemical deposition*, 2nd edn. Wiley, New Jersey
- [http://www.ukasztechnologies.com/?page\\_id=47](http://www.ukasztechnologies.com/?page_id=47)
- Piotrowski T, Sikorski S (2009) *Opto-Electron Rev* 17:252–254
- Chen X, Mao SS (2007) *Chem Rev* 107:2891
- Chen CA, Huang YS, Chung WH, Tsai DS, Tiong KK (2009) *J Mater Sci Mater Electron* 20:S303
- Golubović A, Šćepanović M, Kremenović A, Aškračić S, Berc V, Dohčević-Mitrović Z, Popović ZV (2009) *J Sol-Gel Sci Technol* 49:311–319
- Moulder JF, Stickle WF, Sobol PE, Bomben K (1992) *Handbook of X-ray photoelectron spectroscop*. In: J. Chastain (ed) Perkin-Elmer Corporation 2nd ed (Physical Electronics)



18. NIST X-ray Photoelectron Spectroscopy Database; <http://srdata.nist.gov/xps/>
19. Palik ED (1985) Handbook of optical constants of solids. Academic Press, Boston
20. Alturk Parlak E, Aslı Tumay T, Tore N, Sarioglan S, Kavak P, Turksoy F (2013) Sol Energy Mater Sol Cells 110:58–62
21. Chen X, Zuo L, Fu W, Yan Q, Fan C, Chen H (2013) Sol Energy Mater Sol Cells 111:1–8